Green's function method for dynamic contact calculations

Joseph M. Monti [1,*] Lars Pastewka [2,3] and Mark O. Robbins [1,†]

[1]*Department of Physics and Astronomy, Johns Hopkins University, 3400 North Charles Street, Baltimore, Maryland 21218, USA*

[2]*Department of Microsystems Engineering, University of Freiburg, 79110 Freiburg, Germany*

[3]*Cluster of Excellence livMatS, Freiburg Center for Interactive Materials and Bioinspired Technologies, University of Freiburg, 79110 Freiburg, Germany*

(Received 29 November 2020; accepted 9 April 2021; published 11 May 2021)

Resolving atomic scale details while capturing long-range elastic deformation is the principal difficulty when solving contact mechanics problems with computer simulations. Fully atomistic simulations must consider large blocks of atoms to support long-wavelength deformation modes, meaning that most atoms are far removed from the region of interest. Building on earlier methods that used elastic surface Green's functions to compute static substrate deformation, we present a numerically efficient dynamic Green's function technique to treat realistic, time-evolving, elastic solids. Our method solves substrate dynamics in reciprocal space and utilizes precomputed Green's functions that exactly reproduce elastic interactions without retaining the atomic degrees of freedom in the bulk. We invoke physical insights to determine the necessary number of explicit substrate layers required to capture the attenuation of subsurface waves as a function of surface wave vector. We observe that truncating substrate dynamics at depths that fall as a power of wave vector allows us to accurately model wave propagation without implementing arbitrary damping. The framework we have developed substantially accelerates molecular dynamics simulations of large elastic substrates. We apply the method to single asperity contact, impact, and sliding friction problems and present our preliminary findings.

DOI: 10.1103/PhysRevE.103.053305

I. INTRODUCTION

Mechanical contacts occur in many technical and biological systems, and they determine our experience with our surroundings through touch or when walking. Contact is governed by a balance between the energy gained when making intimate atomic contact and the deformation energy required for surfaces to conform [1,2]. Sophisticated analytical [3–7] and computational [8–12] continuum models have been developed over the last century that accurately describe the deformation energy and contact in the static limit. Those numerical models typically map the subsurface deformation onto the surface degrees of freedom (DOF), leading to a boundary-element formulation [1,13] of the surface's small-strain elastic response. Continuum boundary-element formulations have also been developed for the dynamic (typically viscoelastic) response of a surface within the last decade [14–17].

While continuum contact models accurately depict deformation of solids above the atomic scale, they break down where stresses, strains, and densities change rapidly [18]. On the other hand, molecular dynamics (MD) simulations are a powerful tool commonly used for studying mechanics at atomic scales [19], but can quickly be limited in size and time by computational costs. Yet in contact mechanics, it is often necessary to retain an atomic-level description of the sample while studying long-range elastic deformations [20–22].

The number of DOF in atomic systems of linear dimension L and correspondingly, the computational time per time step of brute force MD simulations, scales with the sample volume L^3. Furthermore, the time to relax the longest wavelength modes grows as L, so the total computational time scales as L^4. Interfacial phenomena such as friction, adhesion, and wear are strongly sensitive to the atomic nature of the interfacial region but also depend on strain fields away from the interface. As a result, a principal challenge for atomic simulations is to resolve the interface while retaining the correct long-range response.

One way to bridge scales in contact mechanics simulations is to couple an atomic treatment of the contact interface where strains may be large with effective descriptions of the bulk where the response is linear. Continuum boundary-element methods exploit the linearity in the small-strain limit to integrate out all bulk DOF and construct a Green's function for the surface's elastic response. In a similar spirit, bulk DOF can be integrated out for full molecular models of crystalline substrates, leading to lattice surface Green's functions [23,24]. Those formulations have proven successful in quickly and efficiently determining the elastic deformation induced by quasistatically applied interfacial forces.

We will here refer to the surface Green's function formulation of crystalline lattices as the contact Green's function (CGF) method [23,24]. In combination with damped dynamics for the relaxation of the system, this method is sometimes termed Green's function molecular dynamics (GFMD)

*Corresponding author: jmonti3@jhu.edu; Present address: Sandia National Laboratories, Albuquerque, New Mexico 87123, USA.

†Deceased.

[23,25–27]. In our approach, the CGF is constructed from a harmonic approximation for lattice vibrations, followed by integrating out DOF far from the region of interest. The harmonic assumption is justified provided that nonlinear behavior is confined to the interfacial domain. CGFs are precomputed in $O(L^2 \ln L)$ time [24] and contribute negligibly to the total simulation run time. The quasistatic response of the system is sufficient for simulations conducted at rates of motion far below the sound speed, for which the substrate is always able to relax before interfacial interactions change. In many scenarios, however, a full dynamical treatment is necessary and in these cases the quasistatic CGF method is inadequate.

In this paper we present a dynamic contact Green's function (DCGF) method for solving time-dependent contact mechanics problems in atomistic settings. In a semi-infinite system, modes with in-plane wave vectors $\vec{q}$ are excited at the surface and propagate into the bulk. Surface modes disperse through phonon-phonon coupling into the continuum of three-dimensional (3D) wave vectors in the bulk, and do not return to the surface. Modes are effectively damped as they move away from the interface. Our approach is motivated by the simple observation that large $q = |\vec{q}|$ modes propagate the shortest distance into solids, while small-q modes persist over large ranges and times.

We note that analytic dynamic Green's functions for semi-infinite substrates have been derived by Kajita *et al.* [28–30], who presented an elegant solution to the time-dependent contact problem without adding explicit damping [29,30]. Their technique differs from ours in that they use a memory kernel to capture subsurface DOF (see also [14–17] for the equivalent continuum formulation). Rather than utilizing a memory kernel, our approach retains the subsurface DOF explicitly but cuts them off as a function of the depth that modes propagate into the solid. To justify this truncation, we add damping to our dynamical equations to model the phonon-phonon interaction. We use Kelvin damping, a momentum-conserving damping scheme similar to dissipative particle dynamics (DPD) [31–33]. There are numerous other techniques for adding physically motivated damping to dynamics [27,28,33–36]. Kelvin damping acts on relative motions between atoms rather than motion itself, a property that respects Galilean invariance. This leads to a dynamic scheme that scales as $L^2 \ln L$ (rather than L^3), or $L^3 \ln L$ (rather than L^4) if we consider relaxation of the longest wavelength modes.

Our formulation has the added benefit that it is straightforward to include thermal fluctuations. We present the relevant stochastic differential equation and derive the corresponding fluctuation-dissipation theorem. While the CGF is able to capture equilibrium thermal fluctuations if combined with an appropriate thermostat [23,37], our approach extends such treatment to dynamical situations. Since we operate in real space, implementation is simple and compatible with existing massively parallel MD software packages, e.g., LAMMPS [38], which we used for the simulations described in this paper.

II. DAMPING OF EXCITED MODES

Dissipation emerges naturally when coarse-graining a molecular system [39], e.g., by partitioning it into a region of interest and a heat-bath region. This dissipation typically takes the form of viscous damping, which in the simplest Markovian incarnation of a drag force on each atom is given by $\vec{F}_i^d = -\gamma(\vec{v}_i - \vec{v}_{\text{ref}})$ where $\vec{v}_i$ is the velocity of atom i and $\vec{v}_{\text{ref}}$ is a reference velocity that is often set to zero. The corresponding relaxation timescale is of order m/γ, where m is the atomic mass, and is independent of the wavelength of the excitation. Viscous damping assigns a reference frame, the laboratory rest frame moving at velocity $\vec{v}_{\text{ref}}$, and therefore violates conservation of momentum and Galilean invariance. The eigenmodes of elastic solids are preserved with weak viscous damping, but all modes are overdamped in the long-wavelength limit [40].

The lowest order combination of spatial and temporal derivatives that satisfies Galilean invariance is Kelvin damping, which adds a force that damps relative velocities between nearby atoms $\vec{F}_i^d = \sum_j \vec{F}_{ij}$ with

$$\vec{F}_{ij} = -\gamma(\vec{v}_i - \vec{v}_j)\theta(|\vec{r}_i - \vec{r}_j|), \tag{1}$$

where $\theta(|\vec{r}_i - \vec{r}_j|)$ is a weighting factor that depends on the distance between atoms and is often set to zero outside the range of atomic interactions. There is no effect on locally homogeneous motion or uniform translations of the sample. For fully 3D wave vectors $\vec{k}$, the rate of energy removed by this type of damping is proportional to k^2 as $k \to 0$. This is most easily seen by writing $\vec{v}_i = \int d^3k\, \vec{v}(\vec{k}) \exp(i\vec{k} \cdot \vec{r}_i)$, which transforms $\vec{F}_i^d = \sum_j \vec{F}_{ij}$ [using Eq. (1)] into

$$\begin{aligned}\vec{F}^d(\vec{k}) &= -\gamma\vec{v}(\vec{k}) \sum_j \left\{1 - \exp(-i\vec{k} \cdot \vec{r}_{ij})\right\}\theta(|\vec{r}_{ij}|) \\ &\approx -\gamma\vec{v}(\vec{k}) \sum_j \left\{i\vec{k} \cdot \vec{r}_{ij} + \frac{1}{2}(\vec{k} \cdot \vec{r}_{ij})^2\right\}\theta(|\vec{r}_{ij}|)\end{aligned} \tag{2}$$

with $\vec{r}_{ij} = \vec{r}_i - \vec{r}_j$. For an isotropic system, $\sum_j \vec{k} \cdot \vec{r}_{ij}\theta(|\vec{r}_{ij}|) \approx 0$ and the leading order dissipation is proportional to k^2. Note that this corresponds to a discrete double spatial derivative and is a general consequence of momentum conservation.

Consequently, long-wavelength modes in solids are always underdamped while short-wavelength modes can be over- or underdamped depending on γ [41]. Note that this is similar to DPD [31–33] which applies the damping force only along the direction between atoms, rather than in all directions. DPD damping also conserves angular momentum while Kelvin damping does not.

In some nonequilibrium MD simulations, it may be desirable to have position-dependent damping. An example is the so-called "stadium damping" technique, wherein the damping coefficient increases in strength away from the interface. This technique has been used with viscous damping in fracture simulations to absorb phonons at the simulation cell boundaries [34]. It is straightforward to make Kelvin damping position dependent by varying the prefactor γ with depth.

All damping schemes can be used to run simulations at finite temperature by implementing suitable random forces as determined by the fluctuation-dissipation theorem [42]. The fluctuation-dissipation theorem relates the temperature to the damping strength and correlations in the random noise. While

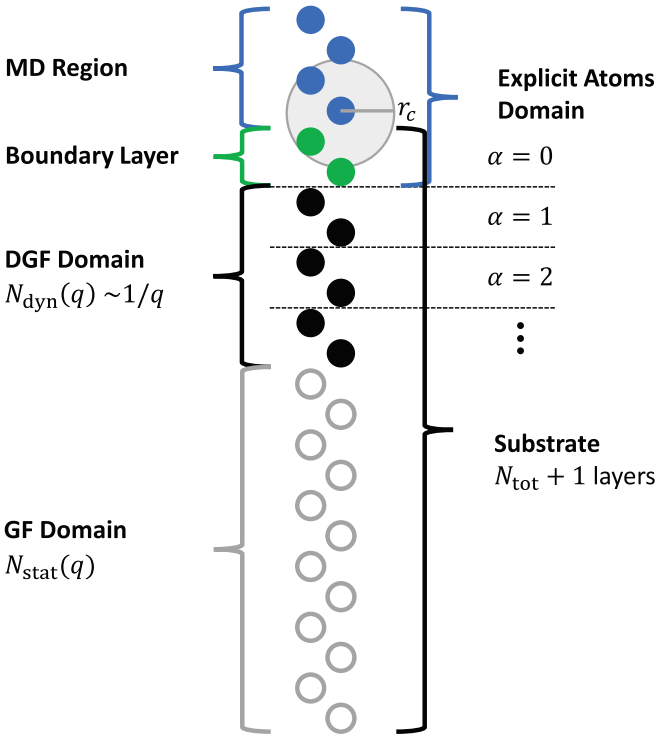

FIG. 1. Decomposition of DCGF method simulations. The topmost region is the MD region treated explicitly. The boundary region must be thicker than r_c (gray, shaded circle) to account for all interactions with explicit atoms. Below the boundary, the total depth N_{tot} is divided into N_{dyn} layers treated using the DCGF method and N_{stat} layers treated using CGF. The precise decomposition of N_{tot} depends upon q.

we focus on athermal systems in this paper, the derivation of a fluctuation-dissipation theorem and the inclusion of finite-temperature fluctuations for the formulation presented here is straightforward and similar to DPD (see Sec. III B) [32].

III. THE DYNAMIC CONTACT GREEN'S FUNCTION METHOD

The DCGF method seeks to alleviate the computational costs of simulating bulk elastic solids in dynamic contact mechanics simulations. Similar to the earlier CGF method [24], this is accomplished by splitting the physical system into a region that is treated exactly and an elastic substrate handled using the harmonic approximation. The simulation is decomposed into three domains as illustrated in the schematic shown in Fig. 1. Each domain is discussed separately below. Note that in all the discussion here, the physical system is a crystal with a free surface.

A. Explicit atoms

The uppermost region in Fig. 1 contains atoms that are explicitly represented in the simulation cell. The explicit atoms domain is composed of the MD region (blue) and the boundary layer (green), which lies on top of the substrate. Atoms in the MD region contribute to the potential energy via arbitrary interactions within the MD region and with atoms in the boundary layer. Interactions between atoms in the MD region with the boundary layer must have a cutoff r_c (shaded gray circle), beyond which the Hessian vanishes. The boundary layer must be larger than r_c to prevent direct interactions with the substrate. Note that for the pair potentials used here, r_c is the cut-off radius of the pair interactions, but for many-body potentials, r_c is generally larger than the cutoff used for the construction of the neighbor list.

The boundary layer bridges the divide between the linear elastic crystalline substrate and any atoms located above. Atoms in the boundary layer are also coupled together by linear elasticity, and interactions between them and the substrate are governed by the harmonic approximation as described below. The dynamics of all atoms in the explicit domain are computed in real space and real time using traditional MD techniques.

B. Harmonic approximation

The substrate is composed of $N_{\mathrm{tot}} + 1$ crystalline layers, including the boundary layer. Each layer is labeled with index $\alpha \leqslant N_{\mathrm{tot}}$; the boundary layer is $\alpha = 0$. With the exception of the boundary layer, atoms in the substrate are not represented explicitly in the simulation cell—as such, they cannot interact directly with atoms above the boundary layer. Rather, substrate atoms are coupled via linearized interactions that facilitate accelerated computation of their dynamics. We additionally choose layers to be thick enough that direct interactions only couple adjacent layers. This simplifies the analytical expressions considerably.

Following the notation of Ref. [24], we invoke the harmonic approximation within the substrate and expand the energy to second order about its equilibrium state. The corresponding dynamical equation of a *damped* harmonic solid is

$$\mathbf{m}\frac{\partial^2 \vec{u}_{i\alpha}}{\partial t^2} + \sum_{j\beta}\left\{\mathbf{D}_{i\alpha j\beta} + \mathbf{G}_{i\alpha j\beta}\frac{\partial}{\partial t}\right\}\vec{u}_{j\beta} = \delta_{0\alpha}\left(\vec{f}_{i0} + \vec{f}_{i0}^{\,\mathrm{exp}}\right), \tag{3}$$

where $\vec{u}_{i\alpha}$ is the displacement of an atom from its equilibrium position. In Eq. (3), $\mathbf{m}$ is diagonal and contains atomic masses, $\mathbf{D}_{i\alpha j\beta}$ is the force-constant matrix that couples atom i in layer α with atom j in layer β, and $\mathbf{G}_{i\alpha j\beta}$ is a matrix that allows for coupled damping between the same atom pairs. The forces on the boundary layer ($\alpha = 0$) from the substrate $\vec{f}_{i0}$ and from the explicit MD domain $\vec{f}_{i0}^{\,\mathrm{exp}}$ do not vanish in general. Note that $\vec{f}_{i0}$ is a constant while $\vec{f}_{i0}^{\,\mathrm{exp}}$ is a function of the positions of the atoms in the explicit atoms domain (see Fig. 1).

Note that Eq. (3) can be turned into a Langevin equation simply by adding a fluctuating random force

$$\vec{f}_{i\alpha}^{\,\mathrm{R}} = \sum_{j\beta}\mathbf{S}_{i\alpha j\beta}\vec{\xi}_{j\beta} \tag{4}$$

to the right-hand side of that equation. Here $\vec{\xi}_{j\beta}$ is a vector of independent white-noise variables and $\mathbf{S}_{i\alpha j\beta}$ is the noise-amplitude matrix. The noise amplitude is related to the dissipation $\mathbf{G}_{i\alpha j\beta}$ by the fluctuation-dissipation theorem [32,42,43]

$$\sum_{k\gamma}\mathbf{S}_{i\alpha k\gamma}\mathbf{S}^{T}_{j\beta k\gamma} = 2k_B T\mathbf{G}_{i\alpha j\beta}, \tag{5}$$

where T is the temperature and k_B is Boltzmann's constant.

To simplify the problem, the system is transformed into Fourier space by using the set of in-plane reciprocal lattice vectors $\vec{q}$ while keeping a real-space representation of the dimension perpendicular to the substrate's surface. This construction decouples the dynamics of the harmonic system for each $\vec{q}$ in the first surface Brillouin zone (BZ). For each wave vector $\vec{q}$, one must solve the dynamics of a chain with $N_{\text{tot}}+1$ nodes, where each node corresponds to a substrate layer with index α.

To frame this more concretely, we now construct the Fourier transform. The real-space lattice vectors that connect unit cells in the boundary layer are $\vec{R}_{i0}$, so that unit cells in lower layers are given by $\vec{R}_{i\alpha}=\vec{R}_{i0}+\alpha\vec{a}$, where $\vec{a}$ is the basis vector between unit cells in neighboring layers. The forward and reverse Fourier transforms of the displacement are as follows:

$$\vec{u}_\alpha(\vec{q},t)=\sum_j \vec{u}_{j\alpha}(t)e^{-i\vec{q}\cdot\vec{R}_{j0}}, \tag{6}$$

$$\vec{u}_{j\alpha}(t)=\int_{\text{BZ}}\frac{d^2q}{A_{\text{BZ}}}\vec{u}_\alpha(\vec{q},t)e^{i\vec{q}\cdot\vec{R}_{j0}}. \tag{7}$$

The sum in the first equation runs over all the unit cells in the boundary layer, while the integral in the second equation is evaluated over the BZ, with area A_{BZ}. Because unit cells are equivalent due to translational invariance, the force-constant and damping matrices only depend on distances between unit cells, given by $\vec{R}_{i0}-\vec{R}_{j0}$ and $\beta-\alpha$. The Fourier transforms of the matrices are

$$\mathbf{D}_{\beta-\alpha}(\vec{q})=\sum_k \mathbf{D}_{j\alpha k\beta}e^{-i\vec{q}\cdot(\vec{R}_{j0}-\vec{R}_{k0})}, \tag{8}$$

$$\mathbf{G}_{\beta-\alpha}(\vec{q})=\sum_k \mathbf{G}_{j\alpha k\beta}e^{-i\vec{q}\cdot(\vec{R}_{j0}-\vec{R}_{k0})}, \tag{9}$$

$$\mathbf{S}_{\beta-\alpha}(\vec{q})=\sum_k \mathbf{S}_{j\alpha k\beta}e^{-i\vec{q}\cdot(\vec{R}_{j0}-\vec{R}_{k0})}. \tag{10}$$

All matrix elements with $|\beta-\alpha|>1$ are zero because the coupling extends only to neighboring layers. The index j vanishes because of in-plane translational invariance. In what follows, we use the shorthand notation $\mathbf{D}_{\alpha\beta}=\mathbf{D}_{\beta-\alpha}$.

In Fourier space, the dynamical equations for each $\vec{q}$ are decoupled and thus block diagonal

$$\sum_\beta\left\{\mathbf{m}\frac{\partial^2}{\partial t^2}\delta_{\alpha\beta}+\mathbf{D}_{\alpha\beta}(\vec{q})+\mathbf{G}_{\alpha\beta}(\vec{q})\frac{\partial}{\partial t}\right\}\vec{u}_\beta(\vec{q},t)$$
$$=\sum_\beta \mathbf{S}_{\alpha\beta}(\vec{q})\vec{\xi}_\beta(\vec{q})+\delta_{\alpha0}\vec{f}_{\text{tot}}(\vec{q},t). \tag{11}$$

Here, $\vec{f}_{\text{tot}}$ is the net force acting on the boundary layer from the substrate and from explicit atoms and $\vec{\xi}_\beta(\vec{q})$ are white-noise variables. The fluctuation-dissipation theorem becomes

$$\sum_\gamma \mathbf{S}_{\alpha\gamma}(\vec{q})\mathbf{S}^\dagger_{\beta\gamma}(\vec{q})=2k_BT\mathbf{G}_{\alpha\beta}(\vec{q}). \tag{12}$$

The elements of $\mathbf{D}_{\alpha\beta}$ and $\mathbf{G}_{\alpha\beta}$ (and thereby $\mathbf{S}_{\alpha\beta}$) depend upon lattice structure, but only a few elements are unique. The $(N_{\text{tot}}+1)\times(N_{\text{tot}}+1)$ force-constant matrix $\mathbf{D}_{\alpha\beta}$ is given in Eq. (10) of Ref. [24] and is reproduced here:

$$\mathbf{D}=\begin{bmatrix}\mathbf{U}'_0 & \mathbf{V} & 0 & \cdots & 0 & 0\\ \mathbf{V}^\dagger & \mathbf{U}' & \mathbf{V} & \cdots & 0 & 0\\ 0 & \mathbf{V}^\dagger & \mathbf{U}' & \cdots & 0 & 0\\ \vdots & \vdots & \vdots & \ddots & \vdots & \vdots\\ 0 & 0 & 0 & \cdots & \mathbf{U}' & \mathbf{V}\\ 0 & 0 & 0 & \cdots & \mathbf{V}^\dagger & \mathbf{U}'_{N_{\text{tot}}}\end{bmatrix}. \tag{13}$$

The damping matrix $\mathbf{G}_{\alpha\beta}$ has a similar tridiagonal form

$$\mathbf{G}=\begin{bmatrix}\mathbf{G}'_0 & \mathbf{H} & 0 & \cdots & 0 & 0\\ \mathbf{H}^\dagger & \mathbf{G}' & \mathbf{H} & \cdots & 0 & 0\\ 0 & \mathbf{H}^\dagger & \mathbf{G}' & \cdots & 0 & 0\\ \vdots & \vdots & \vdots & \ddots & \vdots & \vdots\\ 0 & 0 & 0 & \cdots & \mathbf{G}' & \mathbf{H}\\ 0 & 0 & 0 & \cdots & \mathbf{H}^\dagger & \mathbf{G}'_{N_{\text{tot}}}\end{bmatrix}. \tag{14}$$

Diagonal elements $\mathbf{D}_{\alpha\alpha}$ and $\mathbf{G}_{\alpha\alpha}$ represent the intralayer coupling of layer α. The boundary layer $\alpha=0$ has missing neighbors relative to the $\alpha>0$ layers, and the intralayer coupling elements $\mathbf{U}'_0$ and $\mathbf{G}'_0$ reflect this. Off-diagonal elements $\mathbf{V}$ and $\mathbf{V}^\dagger$, and $\mathbf{H}$ and $\mathbf{H}^\dagger$ represent interlayer coupling of layer α to layers $\alpha+1$ and $\alpha-1$, respectively. All other elements of $\mathbf{D}$ and $\mathbf{G}$ are zero because atoms are only coupled within and between adjacent layers.

The final diagonal elements $\mathbf{U}'_{N_{\text{tot}}}$ and $\mathbf{G}'_{N_{\text{tot}}}$ depend on the choice of boundary conditions at the bottom of the substrate. Free (zero force) boundary conditions correspond to $\mathbf{U}'_{N_{\text{tot}}}=\mathbf{U}'_0$ and $\mathbf{G}'_{N_{\text{tot}}}=\mathbf{G}'_0$, while the rigid (zero displacement) boundary condition is given by $\mathbf{U}'_{N_{\text{tot}}}=\mathbf{U}'$ and $\mathbf{G}'_{N_{\text{tot}}}=\mathbf{G}'$.

C. Reduction of the dynamic degrees of freedom

The equations above fully describe the dynamics of the substrate in the harmonic approximation. The dynamical equation is propagated forward in time for each $\vec{q}$ independently. For each $\vec{q}$, the dynamics is that of a chain with $N_{\text{tot}}+1$ nodes that are free to move in all directions. Solving the full dynamical problem for a cubic box therefore involves $\propto(N_{\text{tot}}+1)^3\propto L^3$ DOF.

Three-dimensional contact mechanics simulations often seek to work in the limit of semi-infinite solids. This limit is typically approximated by using a finite but large N_{tot} to mitigate boundary effects, such as the reflection of pressure waves at boundaries. Computations become prohibitive for large N_{tot} because of the cubic scaling discussed above. We now propose a scheme to reduce the total number of DOF for the dynamical contact problem.

In order to understand the dynamics of excited modes in this system, we consider an infinitely extended 3D crystal. Carrying out the Fourier transform [see Eqs. (8) and (9)] in all three Cartesian directions gives the dynamical equation

$$\{-\mathbf{m}\omega^2+\mathbf{D}(\vec{k})-i\omega\mathbf{G}(\vec{k})\}\vec{u}(\vec{k},\omega)=0, \tag{15}$$

where we have also transformed the time dependency into the Fourier domain. Equation (15) describes a collection of coupled damped harmonic oscillators for each (3D) bulk wave vector $\vec{k}$. We now assume that we can simultaneously diagonalize $\mathbf{D}(\vec{k})$ and $\mathbf{G}(\vec{k})$ with eigenvalues $d(\vec{k})$ and $g(\vec{k})$. (For the specific forms for $\mathbf{D}$ and $\mathbf{G}$ discussed below this is not

possible, but the general discussion still holds.) By virtue of momentum conservation, the asymptotic behavior is given by $d(\vec{k}) = \kappa(ka)^2$ and $g(\vec{k}) = \gamma(ka)^2$ for small k where a is some lattice constant. The admissible values for the wave vectors are therefore

$$(ka)^2 = \frac{m\omega^2}{\kappa - i\omega\gamma}. \tag{16}$$

For a surface excitation with in-plane wave vector $\vec{q}$ and frequency ω, this yields

$$(k_z a)^2 = \frac{m\omega^2}{\kappa - i\omega\gamma} - (qa)^2 \tag{17}$$

for the admissible k_z traveling into the bulk. For static loading ($\omega \to 0$), we obtain $k_z = iq$. This is an evanescent field that decays exponentially in the bulk with a characteristic length $\lambda = 2\pi q^{-1}$. This tells us that deformation can only extend to a depth proportional to the wavelength, a result known as Saint-Venant's principle in the contact mechanics literature [13,44,45].

For dynamic loading at $q > 0$, the imaginary part of $k_z(\omega)$ has a minimum near the frequency that corresponds to the phase velocity of propagating waves, $\omega = cq$, where c is the speed of sound. This minimum describes the wave that decays slowest and hence determines the maximum depth a wave will travel. With $\kappa(q) = \min_\omega \mathrm{Im}[k_z(q,\omega)]$, we find $\kappa(q) \propto q$ for large q. This means Saint-Venant's principle holds even in the dynamic limit.

The observations above suggest that keeping a full description of the N_{tot} substrate layers is unnecessary for all q. If all DOF are retained, $N_{\mathrm{dyn}}(q) = N_{\mathrm{tot}}$, and the DCGF method reduces to the brute force approach. However, since the deformation travels at most down to a depth of order q^{-1}, we can limit the number of layers that we need to explicitly model for each q to a value $N_{\mathrm{dyn}}(q) \leqslant N_{\mathrm{tot}}$. In particular, we can choose $N_{\mathrm{dyn}}(q) \ll N_{\mathrm{tot}}$ for $q \gg 2\pi/L$ without substantially altering the dynamics of the boundary layer. The dynamics of the $N_{\mathrm{tot}} - N_{\mathrm{dyn}}(q)$ nodes at the bottom of the solid are simply discarded (see Fig. 1 for a visual representation of this decomposition). This procedure is only possible because all q chains are independent in the harmonic approximation.

When terminating the q chains, we benefit from the fact that the vast majority of wave vectors are concentrated near the BZ boundary while only a handful of wave vectors are close to $q = 0$. Thus, the lengths of chains for large-q modes comprising the bulk of the substrate DOF can be significantly reduced, while the handful of small-q modes whose dynamics are sensitive to the substrate depth are handled without approximation. The only bookkeeping required is that the minimum number of layers cannot be less than unity, and that the maximum number of layers for $q \to 0$ must be capped. In the simulations for $L \times L$ surfaces discussed below, we use $N_{\mathrm{dyn}}(q > 0) = \max[N_{\mathrm{tot}}(2\pi/L)/q, N_{\mathrm{min}}]$, where $N_{\mathrm{min}} \geqslant 2$ is the smallest allowed number of substrate layers. For simplicity, in most cases we choose $N_{\mathrm{tot}} = L/d_z$ using the layer spacing d_z.

The response to a homogeneous load is determined by $N_{\mathrm{dyn}}(q = 0)$. If $N_{\mathrm{dyn}}(0)$ diverges, the stiffness resisting uniform translations vanishes [10,24]. A practical choice that we opt for is to set $N_{\mathrm{dyn}}(0)$ to the value for the smallest nonzero in-plane wave vector, i.e., $N_{\mathrm{dyn}}(0) = N_{\mathrm{tot}}$. This fixes the substrate reference frame and prevents unbounded translations that would otherwise result from net forces on the (periodic) boundary layer. It effectively models a system with a finite depth of N_{tot} layers.

Care must be taken to ensure that the long-time substrate response is correct. Choosing $N_{\mathrm{dyn}}(q) \propto q^{-1}$ essentially guarantees that all modes have the correct zero-frequency stiffness by Saint-Venant's principle. For completeness, we replace the $N_{\mathrm{stat}}(q) = N_{\mathrm{tot}} - N_{\mathrm{dyn}}(q)$ discarded layers with appropriate effective stiffness matrices $\mathbf{\Phi}(\vec{q})$ obtained by integrating over $N_{\mathrm{stat}}(q)$ layers using the CGF method [24]. (This corresponds to the GF domain in Fig. 1.) Stiffness matrices are computed once at the beginning of the simulation in $O(L^2 \ln L)$ time, resulting in a negligible increase in total run time. The stiffness matrix $\mathbf{\Phi}(\vec{q})$ replaces $\mathbf{U}'_{N_{\mathrm{tot}}}$ as the final entry of $\mathbf{D}$ in Eq. (13) and stitches the two substrate domains together.

The dynamics of the $N_{\mathrm{dyn}}(q)$ layers are computed in reciprocal space but in real time for each $\vec{q}$ using a velocity Verlet algorithm [46]. The DGF domain contributes to the total kinetic energy and to the potential energy within the harmonic approximation. The GF domain only contributes to the potential energy.

D. Kelvin damping

Our choice of $N_{\mathrm{dyn}}(q)$ for each chain is justified if reflections from the ends of shortened chains are negligible. As described above, this is ensured by using Kelvin damping for the dissipation of the energy. Kelvin damping mimics coupling of vibrational modes and thereby thermalization of the system. We can also simply regard it as a means of eliminating reflection from the bottom boundary. As a consequence of Galilean invariance, Kelvin damping acts preferentially on large-q modes without significantly affecting small-q modes.

We include the elements of the damping matrix for nearest-neighbor-coupled fcc lattices. The fcc crystal is oriented with the (110), (1$\bar{1}$0), and (001) directions along the x, y, and z axes, respectively. (The surface normal is along the z axis.) The basis vector connecting unit cells in adjacent layers is then $\vec{a} = d_{\mathrm{nn}}(1/2, 1/2, -1/\sqrt{2})$, where d_{nn} is the nearest-neighbor spacing. We find

$$\mathbf{G}' = \gamma[12 - 2(c_x + c_y)]\mathbf{I}, \tag{18}$$

$$\mathbf{G}'_0 = \gamma[8 - 2(c_x + c_y)]\mathbf{I}, \tag{19}$$

$$\mathbf{H} = -4\gamma c_{x/2} c_{y/2} \exp\left\{i\left(\frac{q_x + q_y}{2}\right)d_{\mathrm{nn}}\right\}\mathbf{I} \tag{20}$$

with $c_x = \cos(q_x d_{\mathrm{nn}})$, $c_{x/2} = \cos(\frac{q_x d_{\mathrm{nn}}}{2})$, and $\mathbf{I}$ is the 3×3 identity matrix. The elements of the force-constant matrix for this lattice structure with atoms interacting via nearest-neighbor springs with spring constant k_b were derived in Ref. [24] and are reproduced for completeness here:

$$\mathbf{U}'(\vec{q}) = k_b \begin{pmatrix} 4 - 2c_x & 0 & 0 \\ 0 & 4 - 2c_y & 0 \\ 0 & 0 & 4 \end{pmatrix}, \tag{21}$$

$$\mathbf{U}_0'(\vec{q}) = k_b \begin{pmatrix} 3-2c_x & 0 & 0 \\ 0 & 3-2c_y & 0 \\ 0 & 0 & 2 \end{pmatrix}, \quad (22)$$

$$\mathbf{V}'(\vec{q}) = k_b \mathbf{v}(\vec{q}) \exp\left\{ i\left(\frac{q_x+q_y}{2}\right) d_{\mathrm{nn}} \right\}, \text{ with}$$

$$\mathbf{v}(\vec{q}) = \begin{pmatrix} -c_{x/2}c_{y/2} & s_{x/2}s_{y/2} & i\sqrt{2}s_{x/2}c_{y/2} \\ s_{x/2}s_{y/2} & -c_{x/2}c_{y/2} & i\sqrt{2}c_{x/2}s_{y/2} \\ i\sqrt{2}s_{x/2}c_{y/2} & i\sqrt{2}c_{x/2}s_{y/2} & -2c_{x/2}c_{y/2} \end{pmatrix}. \quad (23)$$

It is straightforward but tedious to derive **G** for other crystalline structures. (See Ref. [24] for expressions for **D** for other crystalline structures.) In principle, it is possible to allow γ to vary with depth as in stadium damping [34].

E. Parallel scaling and time complexity

Typically, MD simulations are made parallel by decomposing the simulation cell into a grid, with each process owning one piece of the grid [38]. Short-range interactions facilitate the decomposition because atoms on each processor only interact with atoms on processors owning adjacent grid sections. This procedure fails for dynamics in reciprocal space because the Fourier representation couples atomic dynamics over all length scales.

Because Fourier components are decoupled in our simulations, each process can handle a subset of $\vec{q}$ independent of other processes. Communication costs in the DCGF method are primarily associated with collecting all wave vectors to take fast Fourier transforms (FFTs). The forward FFT of the velocities and displacements of the boundary layer and the reverse FFT of the forces on the boundary layer must be calculated each time step, but the time for each calculation is only $\sim L^2 \ln L$. Our implementation carries out parallelization through domain decomposition using a Cartesian decomposition of the surface with equal areas for each domain. The same decomposition is used for the BZ. Improved parallel scaling can be obtained by balancing the number of substrate DOF belonging to each processor for the velocity Verlet integration because more DOF are associated with small q than with large q. This is analogous to load balancing in MD simulations with traditional domain decomposition where the density varies in space.

The total number of DOF after truncating the chains scales as $L^2 \ln L$, a marked reduction from the $O(L^3)$ DOF in the atomic solid. The associated scaling of the computational time is shown in Fig. 2. The time required to relax the longest wavelengths adds an additional scaling factor of L to the computational time, so that the DCGF method scales as $L^3 \ln L$ compared to L^4 scaling for its fully atomic counterpart.

The scaling is essentially unchanged for more aggressive choices of $N_{\mathrm{dyn}}(\vec{q})$, which motivates our choice of $\sim q^{-1}$. Systems with more than 10^6 lattice sites in the boundary layer are easily accessible on just a few processors using the DCGF method, whereas the largest fully atomic simulations are usually limited to much smaller sizes.

In cases where the linear response assumed by the DCGF method is insufficient, it is easy to stack additional lattice planes on top of the boundary region as part of the explicit atoms domain. Atoms in these planes are not governed by the harmonic approximation and can respond nonlinearly. Figure 2 demonstrates that the scaling of the computational time is unaffected provided that the number of added layers is much smaller than N_{tot}. We demonstrate the utility of this approach in later sections.

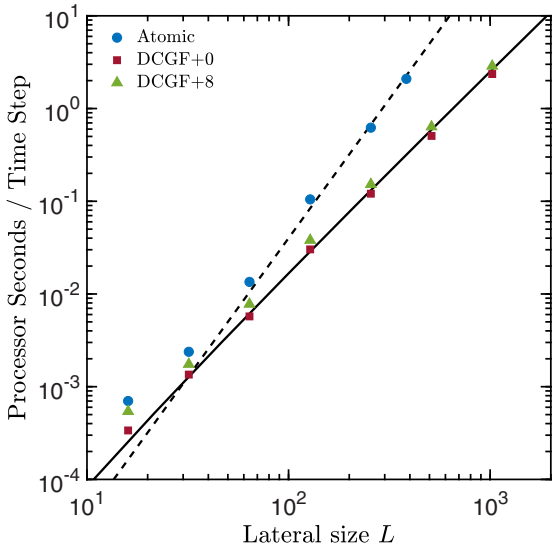

FIG. 2. Comparison of DCGF method and atomic computational time per time step for systems with $L \times L$ atoms in the boundary layer. The fully atomic system contains L^3 atoms and the computational time per time step scales similarly as L^3 (dashed line). DCGF method systems contain L^2 (DCGF+0) and $9L^2$ (DCGF+8) atoms in the MD domain. The corresponding computational time per time step scales as $L^2 \ln L$ (solid line).

IV. EFFECT OF DAMPING PARAMETER ON WAVE PROPAGATION

We have noted that the strength of Kelvin damping depends on wave vector, with long-wavelength modes being essentially undamped. In the absence of other energy scales, the damping parameter can be freely chosen to control the attenuation depth of large q. To illustrate this effect, we show the subsurface attenuation of surface waves with different $\vec{q} = (2\pi/\lambda, 0)$ for an atomic fcc substrate with harmonic bonds. The waves are excited by turning on and then off (pulsing) a small-amplitude force $F_z = f_0 \sin(2\pi x/\lambda)$, where $f_0 \propto [1 - \cos(2\pi t/T)]$. The force is applied over a single period $T \sim d_{nn}/c$ so that the precursor wave propagating with speed c only penetrates one to two layers before the pulse turns off. The amplitude of waves propagating in the solid as a function of depth is calculated by computing $|v_z(q,t)|^2$ for each layer during the time interval prior to the first reflection off the bottom boundary. Then, we identify the depth z_{att} where the maximum amplitude drops below $e^{-3} \approx 0.05$ of the initial value $|v_z(q,0)|^2$ at the surface. The attenuation depth trend was similar for other thresholds, but we found that the results had greater uncertainty for larger thresholds and smaller thresholds required significantly deeper atomic substrates.

Figure 3 illustrates the attenuation of surface waves with increasing wavelength $\lambda = 2\pi/q$ for different damping pa-

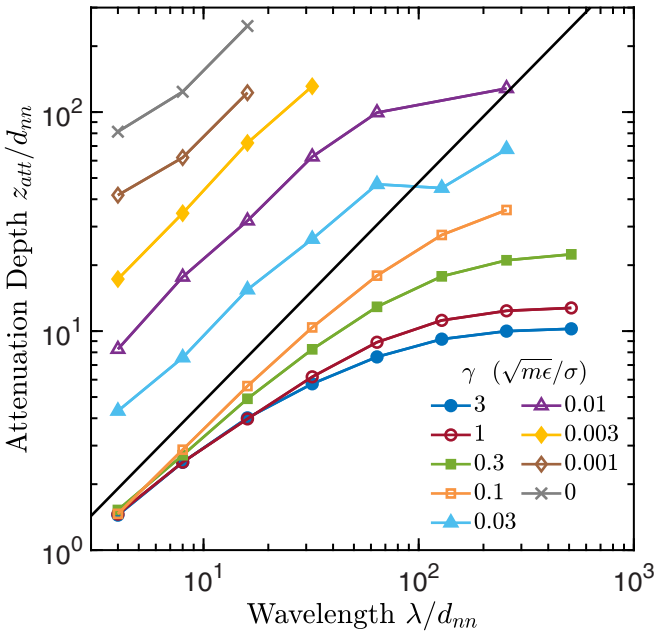

FIG. 3. Depth of the first layer where the kinetic energy of a pulsed surface wave drops below $e^{-3} \approx 0.05$ of the initial surface value as a function of wavelength λ and damping coefficients indicated in the legend. The substrate is fully atomic with Kelvin damping between neighboring atoms, and the boundary layer contains at least $(\lambda/d_{nn}) \times (\lambda/d_{nn})$ lattice sites. The solid line indicates attenuation depth equal to wavelength corresponding to Saint-Venant's principle (see text).

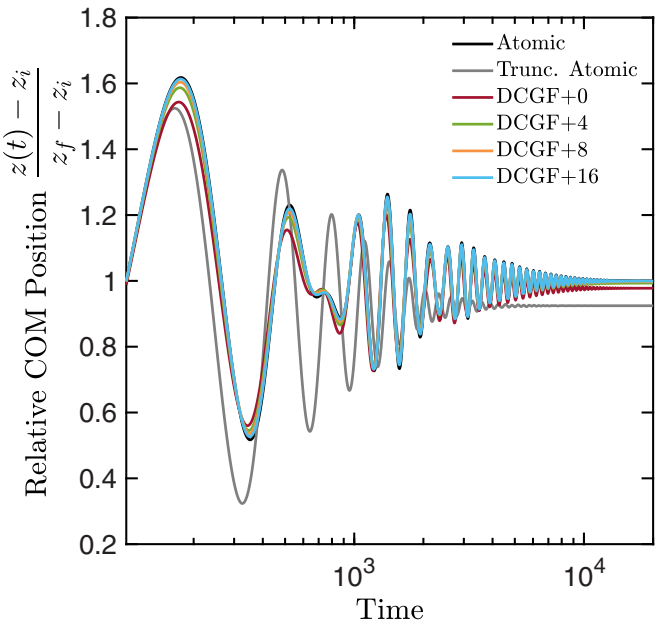

FIG. 4. Center of mass displacement of a rigid disordered sphere under fixed load as a function of time for different DCGF and atomic systems. The reference system is fully atomic (black) with $128 \times 128 \times 129$ mobile lattice sites. z_i is fixed across all simulations and z_f is defined based on the fully atomic system. The denominator $z_f - z_i = -0.54\sigma$ under an applied load of magnitude $5\epsilon/\sigma$. A truncated atomic system (gray) with $128 \times 128 \times 33$ mobile lattice sites is included to emphasize the importance of depth on both dynamic and static properties. Agreement with the atomic result is incrementally improved by stacking additional lattice planes on top of the DCGF boundary layer. DCGF method systems contain 128×128 lattice sites in the boundary layer with the number of additional lattice planes indicated in the legend.

rameters. The attenuation depth scales linearly for small λ irrespective of γ or threshold, although the absolute depth shifts with both. For large γ and λ, the depth saturates at a value much smaller than λ, suggesting that the relative motion between layers is responsible for the rapid attenuation. Note that surface modes attenuate even in the absence of damping due to dispersion into phonons in the full 3D space.

Saint-Venant's principle says that the zero-frequency deformation for wave vectors with magnitude q scales as $\exp(-qz)$. Based on our choice of threshold, z_{att} is the depth where $qz_{\text{att}} = 3$, or $z_{\text{att}}/d_{nn} = 3\lambda/(2\pi d_{nn})$. This is the solid line drawn in Fig. 3, and it is reasonable to consider the regimes above and below the line as the under- and over-damped limits, respectively.

V. COMPARISON WITH ATOMIC SIMULATIONS

In order to demonstrate the efficacy of the DCGF method, we conducted several simulations to directly compare fully atomic calculations with DCGF method calculations. Figure 4 shows results from an example simulation in which a dense, rigid, atomically rough sphere under light load presses into the substrate after starting just out of contact. Atoms in the sphere interact with the substrate using a repulsive truncated Lennard-Jones potential

$$V(r) = 4\epsilon\left[\left(\frac{\sigma}{r}\right)^{12} - \left(\frac{\sigma}{r}\right)^{6}\right], \quad r \leqslant \sqrt[6]{2}\sigma. \tag{24}$$

In this system, the atomic substrate has $128 \times 128 \times 130$ lattice sites and the sphere has a nominal radius of 50σ. The magnitude of the load applied to the sphere is $5\epsilon/\sigma$. Kelvin damping acts opposite to relative velocities between bonded nearest neighbors. The damping coefficient is $\gamma = 1\sqrt{m\epsilon}/\sigma$ to hasten the approach of the sphere to its resting position.

Comparison of the methods is most easily accomplished by showing the evolution of a single coordinate that encapsulates the state of the system. Plotted in Fig. 4 is the change in height $z(t) - z_i$ of the center of mass (COM) of the sphere, where z_i is the initial height, normalized by the final change in height $z_f - z_i$, where z_f is the (mean) resting height of the sphere in the atomic system. Note that results for the DCGF method are also normalized by the height change in the atomic system. The time axis has been shifted to the first crossing point of the resting position to exclude the initial acceleration period before contact, which is identical for all systems. While the sphere COM passes the resting position early on, it oscillates about the final result for an extended duration because long-wavelength modes are excited in the substrate. The fluctuations of long-wavelength modes are unavoidable with Kelvin damping but do not influence time-averaged dynamics. They are absent for quasistatic loading. To highlight the importance of resolving long-wavelength modes, we also include a truncated atomic system with $128 \times 128 \times 34$ lattice sites.

The DCGF method computes the dynamics of the boundary layer assuming linear response, but surface displacements

are usually significant in contact simulations. In order to better capture nonlinear behavior at the surface, we can treat more layers of the crystal explicitly. These additional layers are coupled to each other and the boundary layer using the same bonding and damping schemes as the fully atomic system. The number of layers in the harmonic region is reduced by the same number of layers. While the bare DCGF method (DCGF+0) captures the features of the sphere dynamics, Fig. 4 shows that simulating more layers explicitly progressively improves the DCGF result. There is a similar shift in the accuracy of the resting position. Careful consideration is needed to weigh the additional computational costs of simulating more lattice planes against the accuracy of the nonlinear response.

VI. DEMONSTRATION OF ERROR

Quantifying error between the DCGF method and atomic computation is challenging because the set of dynamical variables is large. Even in a nominally deterministic system like the bouncing sphere discussed above, there are deviations between simulations that decorrelate over time. To circumvent this issue, we present a slight variant of the test above to illustrate how additional lattice planes reduce the deviations of the DCGF method from atomic calculations. In this system, the *unloaded* sphere travels with a prescribed initial velocity $\vec{v} = -v_i\hat{z}$ into contact, after which it rebounds to infinity. The initial speed v_i is varied to control the dynamics of the impact. All other interactions are the same as described above for the bouncing sphere.

The substrate imposes a force $\vec{F}$ on the COM of the sphere that acts to slow it down and reverse its momentum. The impulse responsible for the change in momentum is dominated by the perpendicular force component F_z, which is always positive and has a pulselike shape during the collision. The final speed of the sphere is $v_f = \sqrt{\vec{v}_f \cdot \vec{v}_f}$ and the coefficient of restitution is defined as $C_R = v_f/v_i$. In-plane force components and resulting in-plane velocities are small so that $v_f \approx v_{z,f}$. In a perfectly elastic collision, $C_R = 1$, but our simulations treat viscoelastic solids with internal damping that dissipates some of the initial total energy.

To provide an estimate of the reliability of the DCGF method, we computed the maximum change in bond length found in the fully atomic system, which gives a sense of the peak strain during the collision. The largest change in bond length always coincided with the most compressed bond and grew with the initial speed. The relative error of C_R versus maximum bond length change is plotted in Fig. 5. The figure shows that even the DCGF+0 system performs well when bonds are compressed only a few percent but the error grows substantially with greater changes in bond length. Error is reduced by introducing additional lattice planes—from about 2% to close to 0.05% in the low strain regime by adding up to 32 planes—and can be made arbitrarily small with more lattice planes. When the maximum bond length change approached 9% for an impact depth $\sim 0.12R$, the similarity in the errors for the DCGF+8, DCGF+16, and DCGF+32 systems suggests that even 32 additional lattice planes are insufficient to fully capture nonlinearities. Nonetheless, the error only reached ~1% despite the large strain imposed during the collision, demonstrating the efficacy of the DCGF method outside the light load limit.

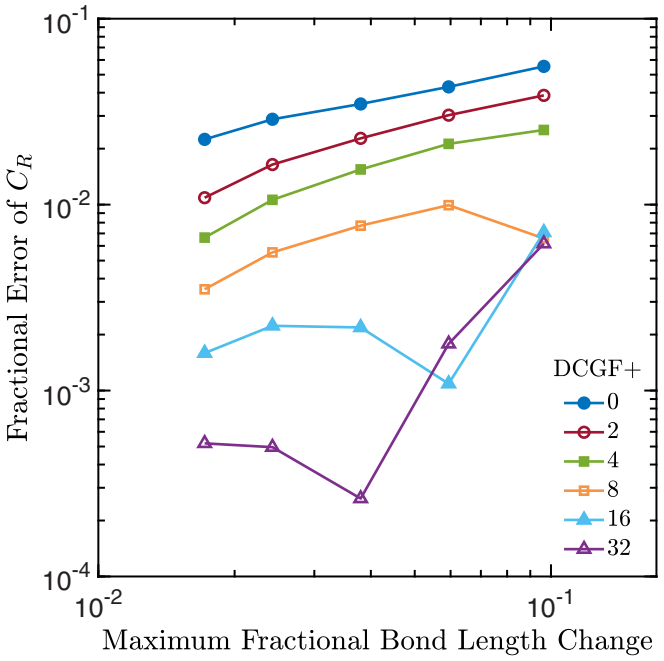

FIG. 5. Fractional error in the coefficient of restitution for the DCGF method compared to a fully atomic system with 128 × 128 × 129 mobile lattice sites. DCGF method systems contain 128 × 128 lattice sites in the boundary layer with the number of additional lattice planes indicated in the legend. The system is a rigid disordered sphere with variable initial velocity perpendicular to the boundary. The sphere rebounds away after contact. Bond length changes are measured in the atomic system, and always corresponded to the most compressed bond.

VII. APPLICATION TO SLIDING FRICTION

Static friction is the lateral force required to initiate sliding between objects, while kinetic friction refers to the time-averaged force required for steady sliding. The CGF method and related techniques have been applied to the problem of the static friction and quasistatic sliding of nanoscale contacts [21,22,27,47]. Here, we focus on kinetic friction and in particular, viscous friction. Viscous friction is a friction law that relates the kinetic friction force to sliding velocity as $F_k \propto v$, such that F_k vanishes at zero velocity, i.e., there is no static friction [48–50].

We seek to study the kinetic friction on a one-dimensional (1D) sinusoidal potential sliding over an elastic fcc solid with nearest-neighbor coupling k_b using the DCGF method. The sliding potential imposes a lateral force $F_x = f_0 \sin[2\pi/\lambda(x - vt)]$ to the $L \times L$ DCGF boundary layer. Note that the force acts in the direction of sliding. As a result, the force on each substrate atom is homogeneous across the y axis. We report the kinetic friction force F_k normalized by the total mass of the surface layer $M = m(L/d_{nn})^2$, where m is the mass of an atom. The substrate side length L is always a multiple of λ, and $\lambda \geqslant 4d_{nn}$. The typical atomic displacements $\Delta \equiv f_0/k_b \ll d_{nn}$, so linear response is valid here.

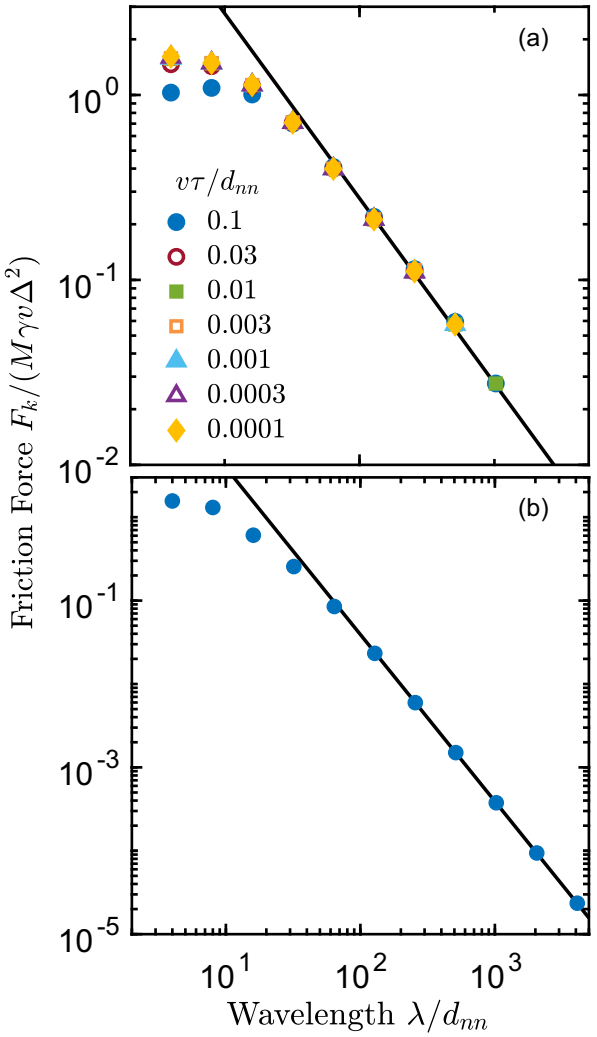

FIG. 6. Kinetic friction per unit length imposed by the 1D sinusoidal potential moving along $\hat{x}$ as a function of wavelength. The friction is normalized by the damping parameter and sliding speed. (a) Kinetic friction on 3D substrates with sliding speeds indicated in the legend. The solid line indicates $F_k \propto \lambda^{-1}$. (b) Kinetic friction on effectively 2D substrates with sliding speed $v = 0.01 d_{nn}/\tau$. The solid line indicates $F_k \propto \lambda^{-2}$.

A stationary wave with $v = 0$ exerts zero total force on the substrate when atoms are located at their equilibrium positions. For $v > 0$, instantaneous atomic displacements lead to a net force on the boundary layer. The kinetic friction force is the negative of the total force imposed on the boundary layer. We compute F_k by calculating the mean force after long sliding times, well after the initial transient period.

To test the effect of substrate depth on the kinetic friction, we ran simulations with large depth ($L/d_{nn} = 1024, N_{\rm tot} = 1024$) and small depth ($L/d_{nn} = 4096, N_{\rm tot} = 4$), representative of bulk and quasi-2D substrates, respectively. Simulation results are shown for different v and λ in Fig. 6(a) (bulk) and 6(b) (quasi-2D). For any given set of parameters, we found viscous friction when the sliding velocity was smaller than about $0.1c$, resulting in a universal curve for $F_k/\gamma v$. As expected from linear response theory, F_k was proportional to Δ^2 [49,50].

Perhaps the most interesting dependence shown in Fig. 6 is the scaling with wavelength λ. There is relatively little dependence on wavelength for small λ, but both deep and shallow substrates show power-law decays in F_k for wavelengths larger than about $20 d_{nn}$. We observed that the crossover behavior shifted to larger λ with increasing γ. Kelvin damping yields $F_k \propto q^2 \sim \lambda^{-2}$ for large λ, but we instead find that $F_k \propto \lambda^{-1}$ for deep substrates. For thin substrates, all atoms contribute to Kelvin damping down to a constant (small) depth for all λ, yielding the expected λ^{-2} dependence. However, for deep substrates the deformation extends down to distances of order λ. For sufficiently small velocities, the deformation simply translates along with the surface excitation and there is no emission of waves into the bulk [51]. This means that the volume from which dissipation emerges is proportional to λ for deep substrates while it is constant for shallow substrates. Thus, the kinetic friction force for deep substrates rises by the same factor compared to shallow ones. This argument also holds for shallow substrates when λ is smaller than the depth, explaining the similarity of F_k for panels (a) and (b) for $\lambda \leqslant 8$.

VIII. CONCLUSIONS

In this paper, we have outlined the DCGF method for accelerating simulations of elastic solids. Using a 2D Fourier decomposition of the top plane of a crystalline solid and a real-space representation of the perpendicular direction, we compute the dynamics of a linear elastic substrate in real time. In the harmonic approximation, the dynamics of each surface wave vector $\vec{q}$ are decoupled and may be solved as a chain of nodes corresponding to layers in the substrate. By leveraging the fact that large-q modes disperse rapidly in solids, we demonstrated that q chains can be terminated at successively smaller depths with increasing q without significantly altering the dynamics at the surface. To that end, we incorporated Kelvin damping in our methodology as a model for phonon-phonon coupling which prevents reflections for large-q modes with foreshortened q chains. We presented the associated damping matrices for Kelvin damping of an fcc (001) surface with nearest-neighbor coupling. We also discussed how finite temperature calculations are possible within the present scheme and derived the fluctuation-dissipation theorem for the underlying Langevin equation.

As a result of the chain-termination procedure, the total number of degrees of freedom and resultant computational time per time step are $O(L^2 \ln L)$ rather than $O(L^3)$, meaning that the DCGF method allows for the simulation of much larger substrates than conventional brute force MD simulations. This also implies a similar acceleration factor for the computational time to relax long-wavelength modes compared to brute force MD [$O(L^4)$ reduces to $O(L^3 \ln L)$].

In cases where linear response is inadequate to study interfacial dynamics, we showed that nonlinear behavior can still be captured by stacking additional lattice planes on top of the DCGF boundary layer. In particular, this procedure allows for the study of surface plasticity provided that the plastic zone is confined to the explicitly represented lattice planes.

We provided guidelines for the attenuation of surface modes away from the interface based on Kelvin damping strength and gave examples of error compared to atomic simulations based on the maximum change in bond length. Finally, we demonstrated that Kelvin damping leads naturally to a viscous friction law for a sliding sinusoidal potential in the unpinned limit. For shallow substrates, the kinetic friction force exhibited the expected q^2 scaling resulting from Kelvin damping. For deep substrates, the kinetic friction instead scaled as q as a result of the extra volume available to dissipate energy within the bulk, leading to higher friction forces compared to the shallow substrate.

ACKNOWLEDGMENTS

We thank Jan Grießer for useful discussions and the DAAD for support for a short visit of J.M. to Freiburg. This material is based on work supported by the National Science Foundation (Grants No. DMR-1411144 and No. DMR-1929467), the European Commission (Marie-Curie IOF-272619), and the Deutsche Forschungsgemeinschaft (DFG, Grant No. PA 2023/2). Computations were carried out on the Johns Hopkins University Homewood High Performance Cluster, the Maryland Advanced Research Computing Center and NEMO at the University of Freiburg (DFG Grant INST 39/963-1 FUGG).

[1] K. L. Johnson, *Contact Mechanics* (Cambridge University Press, Cambridge, UK, 1985).
[2] B. N. J. Persson, O. Albohr, U. Tartaglino, A. I. Volokitin, and E. Tosatti, J. Phys.: Condens. Matter **17**, R1 (2004).
[3] B. Derjaguin, Kolloid Z. **69**, 155 (1934).
[4] K. L. Johnson, K. Kendall, and A. D. Roberts, Proc. R. Soc. Lond. A **324**, 301 (1971).
[5] B. V. Derjaguin, V. M. Muller, and Y. P. Toporov, J. Colloid Interf. Sci. **53**, 314 (1975).
[6] B. N. J. Persson, J. Chem. Phys. **115**, 3840 (2001).
[7] B. N. J. Persson, Phys. Rev. Lett. **87**, 116101 (2001).
[8] J. J. Kalker and Y. Randen, J. Eng. Math. **6**, 193 (1972).
[9] J. J. Kalker, Commun. Appl. Numer. M. **2**, 401 (1986).
[10] H. Stanley and T. Kato, J. Tribol. **119**, 481 (1997).
[11] I. Polonsky and L. Keer, Wear **231**, 206 (1999).
[12] L. Pei, S. Hyun, J. Molinari, and M. Robbins, J. Mech. Phys. Solids **53**, 2385 (2005).
[13] C. L. Amba-Rao, J. Franklin Inst. **287**, 241 (1969).
[14] G. Carbone and C. Putignano, J. Mech. Phys. Solids **61**, 1822 (2013).
[15] K. E. Koumi, D. Nelias, T. Chaise, and A. Duval, Mech. Mater. **77**, 28 (2014).
[16] S. Kusche, ZAMM **97**, 226 (2017).
[17] R. Bugnicourt, P. Sainsot, N. Lesaffre, and A. Lubrecht, Trib. Int. **113**, 279 (2017).
[18] B. Luan and M. O. Robbins, Nature (London) **435**, 929 (2005).
[19] E. B. Tadmor and R. E. Miller, *Modeling Materials: Continuum, Atomistic and Multiscale Techniques* (Cambridge University Press, Cambridge, UK, 2011).
[20] M. Ma, A. Benassi, A. Vanossi, and M. Urbakh, Phys. Rev. Lett. **114**, 055501 (2015).
[21] T. A. Sharp, L. Pastewka, and M. O. Robbins, Phys. Rev. B **93**, 121402(R) (2016).
[22] T. A. Sharp, L. Pastewka, V. L. Lignères, and M. O. Robbins, Phys. Rev. B **96**, 155436 (2017).
[23] C. Campañá and M. H. Müser, Phys. Rev. B **74**, 075420 (2006).
[24] L. Pastewka, T. A. Sharp, and M. O. Robbins, Phys. Rev. B **86**, 075459 (2012).
[25] C. Campañá and M. H. Müser, Europhys. Lett. **77**, 38005 (2007).
[26] C. Campañá, M. H. Müser, and M. O. Robbins, J. Phys.: Condens. Matter **20**, 354013 (2008).
[27] Y. Zhou, M. Moseler, and M. H. Müser, Phys. Rev. B **99**, 144103 (2019).
[28] S. Kajita, H. Washizu, and T. Ohmori, Phys. Rev. B **82**, 115424 (2010).
[29] S. Kajita, H. Washizu, and T. Ohmori, Phys. Rev. B **86**, 075453 (2012).
[30] S. Kajita, Phys. Rev. E **94**, 033301 (2016).
[31] P. J. Hoogerbrugge and J. M. V. A. Koelman, Europhys. Lett. **19**, 155 (1992).
[32] P. Español and P. B. Warren, Europhys. Lett. **30**, 191 (1995).
[33] T. Soddemann, B. Dünweg, and K. Kremer, Phys. Rev. E **68**, 046702 (2003).
[34] B. L. Holian and R. Ravelo, Phys. Rev. B **51**, 11275 (1995).
[35] W. Cai, M. de Koning, V. V. Bulatov, and S. Yip, Phys. Rev. Lett. **85**, 3213 (2000).
[36] W. E and Z. Huang, Phys. Rev. Lett. **87**, 135501 (2001).
[37] Y. Zhou, A. Wang, and M. H. Müser, Front. Mech. Eng. **5**, 67 (2019).
[38] S. Plimpton, J. Comput. Phys. **117**, 1 (1995).
[39] R. W. Zwanzig, *Nonequilibrium Statistical Mechanics* (Oxford University Press, New York, 2001).
[40] M. Müser, *Computer Simulations in Condensed Matter Systems: From Materials to Chemical Biology Volume 2*, edited by M. Ferrario, G. Ciccotti, and K. Binder, Lecture Notes in Physics (Springer, Berlin, Heidelberg, 2006), Vol. 704, pp. 367–406.
[41] M. Salerno, Inertia and the Critical Scaling of Avalanches in Sheared Disordered Solids, Ph.D. thesis, Johns Hopkins University, 2013.
[42] C. W. Gardiner, *Handbook of Stochastic Methods*, Synergetics (Springer, Berlin, Heidelberg, 2004).
[43] M. Grmela and H. C. Öttinger, Phys. Rev. E **56**, 6620 (1997).
[44] A. E. H. Love, *A Treatise on the Mathematical Theory of Elasticity* (Cambridge University Press, Cambridge, UK, 1906).
[45] P. Sainsot, Proc. Inst. Mech. Eng., Part C **225**, 274 (2011).
[46] M. P. Allen and D. J. Tildesley, *Computer Simulation of Liquids* (Oxford University Press, New York, 1989).
[47] J. M. Monti and M. O. Robbins, ACS Nano **14**, 16997 (2020).
[48] J. Krim and A. Widom, Phys. Rev. B **38**, 12184 (1988).
[49] M. Cieplak, E. D. Smith, and M. O. Robbins, Science **265**, 1209 (1994).
[50] E. D. Smith, M. O. Robbins, and M. Cieplak, Phys. Rev. B **54**, 8252 (1996).
[51] L. Landau, E. Lifshitz, A. Kosevich, J. Sykes, L. Pitaevskii, and W. Reid, *Theory of Elasticity: Volume 7*, Course of Theoretical Physics (Elsevier Science, Netherlands, 1986).